ACS APPLIED ELECTRONIC MATERIALS

pubs.acs.org/acsaelm Article

Ultraflexible and Transparent $MoS_2/\beta\text{-}Ga_2O_3$ Heterojunction-Based Photodiode with Enhanced Photoresponse by Piezo-Phototronic Effect

Madan Sharma, Arunima Singh, Ashok Kapoor, Aditya Singh, Bhera Ram Tak, Shuchi Kaushik, Saswata Bhattacharya, and Rajendra Singh*

Cite This: https://doi.org/10.1021/acsaelm.3c00120 Read Online

ACCESS | Metrics & More | Article Recommendations | Supporting Information

ABSTRACT: Two-dimensional material-based flexible devices are extremely suitable for smart, portable, and wearable applications. However, the inevitability of substrate strain, which significantly affects device performance, makes it difficult to get a flexible device to function efficiently. Herein, for the first time, we report a flexible $MoS_2/\beta\text{-}Ga_2O_3$ broadband photodiode with an enhancement in the photocurrent and responsivity with bending. The electrical analysis of the heterojunction demonstrated excellent photoresponse characteristics with a photo-to-dark current ratio of 10^3, even at low power density. Compared to strain-free conditions, the device showed an enhancement in the photocurrent and responsivity by 155% and 136%. Based on the piezo-phototronic effect, the band structure at the heterojunction interface is modified by the piezo-potential caused by applied strain, which also widens the depletion region. The wider depletion can be employed discretely to increase photogenerated carrier separation and transport, improving photoresponse performance. The bending durability and robustness of the photodiode were also investigated at 500 bending cycles and high temperatures. The band alignment of the heterojunction was determined before fabricating the flexible photodiode. The junction showed straddling (type I) band alignment, with a valence band offset (ΔE_V) of 2.28 eV and a conduction band offset (ΔE_C) of 0.73 eV, as validated by first-principles calculations. This research paves the path for strain-tunable vdW heterojunctions, which might lead to the invention of flexible optoelectronic devices.

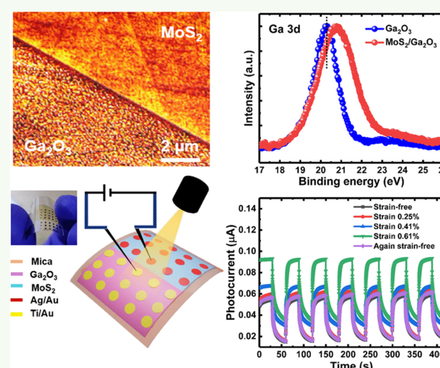

KEYWORDS: *2D materials, flexible photodetector, piezo-phototronic effect, MoS_2/Ga_2O_3 heterostructures, transparent photodetector, strain-tunable vdW heterojunctions*

Downloaded via INDIAN INST OF TECH DELHI- IIT on April 5, 2023 at 12:00:36 (UTC).
See https://pubs.acs.org/sharingguidelines for options on how to legitimately share published articles.

1. INTRODUCTION

Flexible electronics have brought attention due to widespread applications, such as wearable sensors,[1] artificial e-skin,[2] and smart, portable, and low-cost disposable devices.[3] Flexible devices with high performance, excellent mechanical deformability, and integrated functionality are desirable to drive the next-generation flexible electronics. Transition metal dichalcogenides (TMDCs) are potential materials for flexible electronics due to their extraordinary layer-dependent electronic, optical, and mechanical properties. Atomically thin TMDCs like molybdenum disulfide (MoS_2), tungsten disulfide (WS_2), and molybdenum diselenide ($MoSe_2$) have high charge mobilities, large Young modulus, good optical transparency, and high strain limit, which make them suitable candidates for the high-performance flexible devices.[4,5] MoS_2 is one of the most researched 2D semiconducting material among all the TMDCs due to its unique properties such as tunable bandgap, strong spin−orbit coupling, and availability of unsaturated d-orbitals.[6,7] Further, due to its wide spectrum response, a large density of states, increased carrier mobility, and high absorption rate of incoming photons, few-layer MoS_2 appears to be more appealing than monolayer MoS_2, particularly for optoelectronic applications.[8−10] On flexible polymer-based substrates, it is difficult to improve performance due to inherent substrate strain, the limitations of transfer techniques, and complicated production. Because of the piezoresistive effect, stress concentration, and stress softening, strain from a flexible substrate has a significant impact on the performance of the device for flexible optoelectronics. Few studies on 2D material-based flexible devices have been reported recently in which the influence of strain has been minimized.[11,12] Our research intends to increase the perform-

Received: January 26, 2023
Accepted: March 15, 2023

ACS Publications © XXXX American Chemical Society

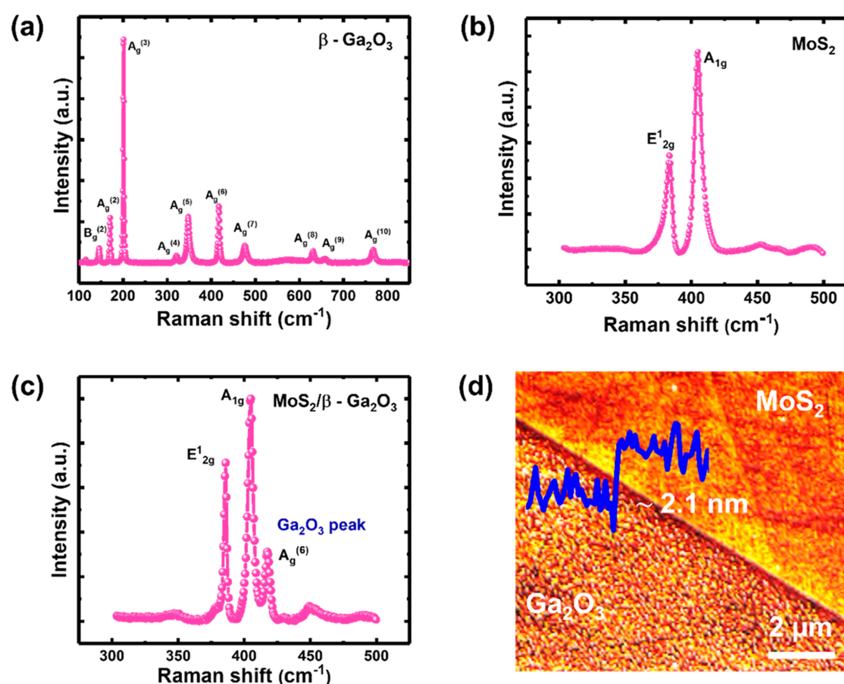

Figure 1. Raman spectrum of (a) β-Ga_2O_3, (b) trilayer MoS_2, and (c) the MoS_2/β-Ga_2O_3 heterostructure. (d) AFM image of the MoS_2/β-Ga_2O_3 heterostructure.

ance of photodetectors based on the piezoelectric effect in trilayer MoS_2 by using the inevitable substrate strain.

Due to its non-centrosymmetric structure, a piezoelectric effect in MoS_2 with an odd number of atomic layers was recently described, which might be exploited to vary the height of the Schottky barrier in metal−semiconductor contacts and/or power nanodevices.[13,14] To improve the performance of optoelectronic devices such as photodetectors, LEDs, and solar cells, the piezo-phototronic effect uses the piezopotential to regulate carrier production, transport, separation, and/or recombination.[15−19] For example, Fei Xue et al.[20] fabricated a pressure-modulated MoS_2/GaN heterojunction photodiode (response time ∼66 ms) based on the piezo-phototronic effect. Pengwen Guo et al.[18] achieved high photoresponsivity in MoS_2 by the flexophototronic effect. They have developed a novel 3D stress-stabilization process to generate permanent polarization in MoS_2. The intriguing characteristics of heterojunctions, such as the controllable charge-depletion layer and dangling-bond-free surface, have reignited interest in new interesting physics at the 2D/3D interfaces.[21] The performance of light-harvesting devices and high-speed electronics has been significantly improved because of these heterojunctions.[22]

Gallium oxide (Ga_2O_3), an emerging semiconducting material, has wide application areas such as deep ultraviolet (DUV) solar-blind photodetectors,[23] high-power Schottky diodes and transistors,[24] transparent conducting oxides (TCO),[25] and resistive switching[26] because of its ultrawide bandgap and better material properties than other wide-bandgap materials (SiC, GaN, etc.). The β-Ga_2O_3, which has a monoclinic crystal structure and bandgap of ∼4.5−4.9 eV, is the most thermally stable among the five known phases (α, β, γ, δ, and ε). It is also chemically, mechanically, and thermally stable at high temperatures. β-Ga_2O_3 is intrinsically solar-blind due to its ultrawide bandgap, which corresponds to a peak wavelength of ∼250 nm. Furthermore, due to its large bandgap, β-Ga_2O_3-based diodes and field-effect transistors (FETs) can have outstanding power device features such as high power, high breakdown voltage, and low loss.[27−30] For incorporating the respective benefits of both the existing 2D and 3D materials, the integration of MoS_2 with β-Ga_2O_3 is of significant interest. The interfacial energy and band alignment affect the optical and electrical characteristics of 2D/3D heterojunctions. As a result, variable band alignments are highly sought for increasing the performance of heterojunction-based devices. Until now, minimal reports have been published on the MoS_2/β-Ga_2O_3 heterojunction, with no report on its corresponding flexible photodetector.[31,32]

Herein, we first extensively studied the band alignment of the MoS_2/β-Ga_2O_3 heterojunction via high-resolution X-ray photoelectron spectroscopy (HR-XPS) and first-principles calculations. Following that, a flexible photodiode was built onto the MoS_2/β-Ga_2O_3 heterojunction to achieve good optoelectronic performance via a piezo-phototronic effect. The flexible photodiode gave a high photoresponse with a photo-to-dark current ratio (PDCR) of 10^3 and detection sensitivity of 2.4 × 10^{11} Jones. The high-temperature performance of the photodiode was investigated from RT to 125 °C. Temperature-dependent PDCR and temporal response characteristics show that the photodiode can be operated in high-temperature environments. This experimental investigation is expected to give a deeper knowledge of 2D/3D heterostructures as well as guidelines for industrial applications of flexible photodetectors.

2. RESULTS AND DISCUSSION

To begin with, the structural information on both materials was confirmed using Raman spectroscopy. As shown in Figure 1a, the Raman spectrum of Ga_2O_3 includes a number of different vibrational modes: $B_g^{(2)}$ = 145.6 cm^{-1}, $A_g^{(2)}$ = 170.5 cm^{-1}, $A_g^{(3)}$ = 201.0 cm^{-1}, $A_g^{(4)}$ = 320.7 cm^{-1}, $A_g^{(5)}$ = 347.4 cm^{-1}, $A_g^{(6)}$ = 416.4 cm^{-1}, $A_g^{(7)}$ = 475.0 cm^{-1}, $A_g^{(8)}$ = 630.8 cm^{-1}, $A_g^{(9)}$ = 658.9 cm^{-1}, and $A_g^{(10)}$ = 766.0 cm^{-1}, all of which

https://doi.org/10.1021/acsaelm.3c00120
ACS Appl. Electron. Mater. XXXX, XXX, XXX−XXX

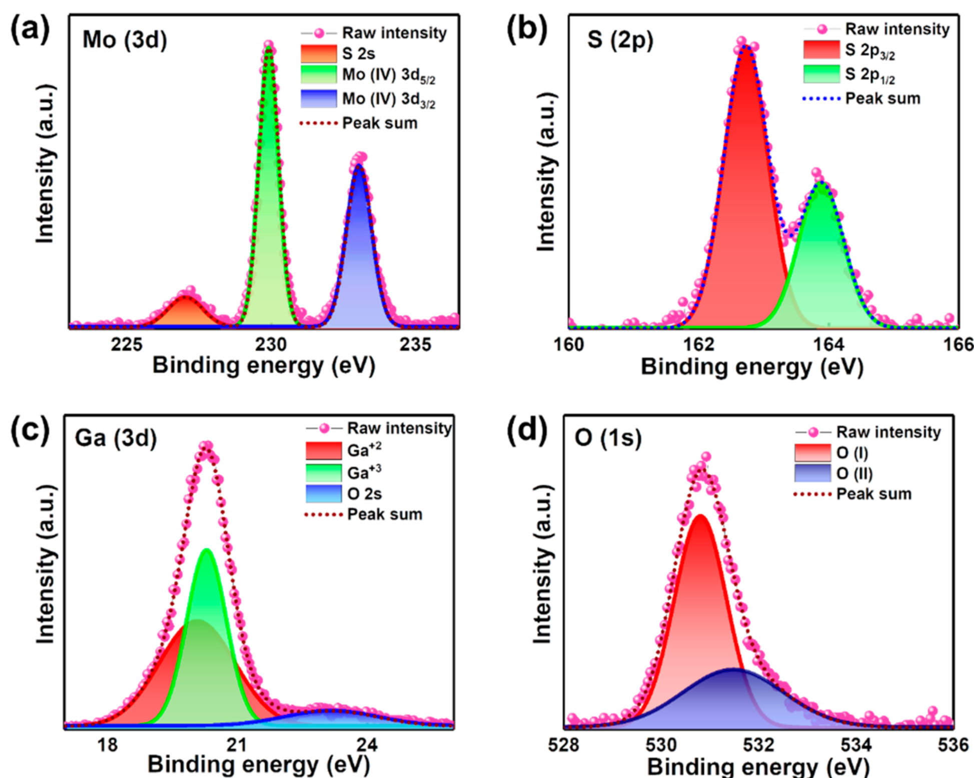

Figure 2. Core-level XPS spectra of (a) Mo 3d, (b) S 2p, (c) Ga 3d, and (d) O 1s.

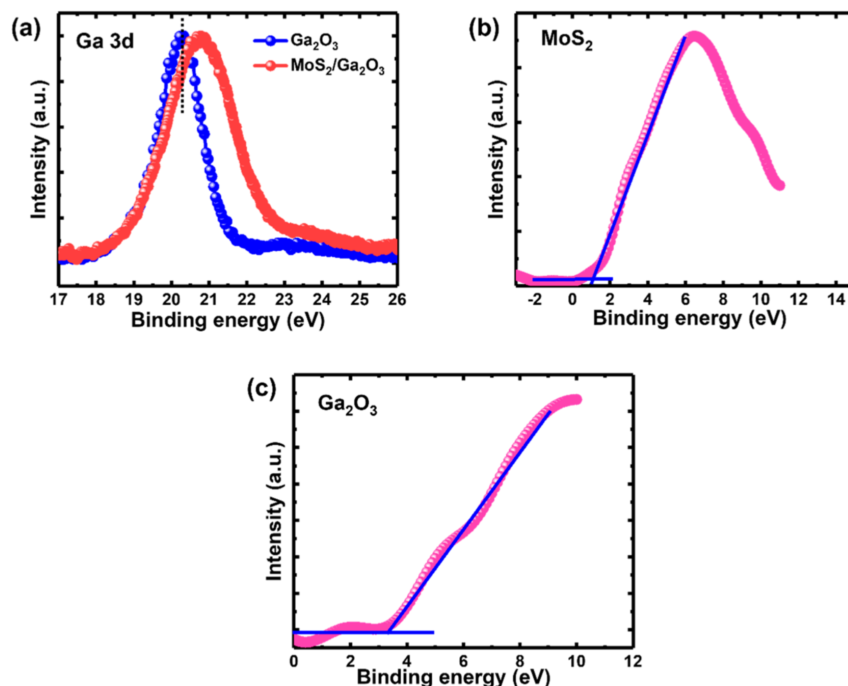

Figure 3. (a) XPS spectra of the Ga 3d core level for pristine β-Ga_2O_3 and MoS_2/β-Ga_2O_3. Valence band spectra of (b) MoS_2 and (c) β-Ga_2O_3.

are consistent with the previous reports of a beta-phase material.[33,34] The peak position of E^1_{2g} and A_{1g} modes of MoS_2 was observed at 383.07 and 405.18 cm^{-1}, respectively (Figure 1b). The peak difference ($\Delta\omega$) between E^1_{2g} and A_{1g} modes was 22.11 cm^{-1}, showing that the as-grown MoS_2 is trilayer (3L).[35] Figure 1c is the Raman spectra of the MoS_2/β-Ga_2O_3 heterostructure, which clearly shows the E^1_{2g} and A_{1g} modes of MoS_2 and the $A_g^{(6)}$ mode of β-Ga_2O_3. The AFM topography of the MoS_2/β-Ga_2O_3 heterostructure is shown in Figure 1d. The thickness of MoS_2 was found to be 2.1 nm, indicating that the MoS_2 is trilayer (3L).

2.1. Band Alignment of the MoS_2/β-Ga_2O_3 Heterostructure. XPS was used to explore the band alignment of the MoS_2/β-Ga_2O_3 heterostructure. Mo 3d and Ga 3d core levels (CLs) were utilized to analyze the valence band offset (VBO, ΔE_V) and conduction band offset (CBO, ΔE_C). The

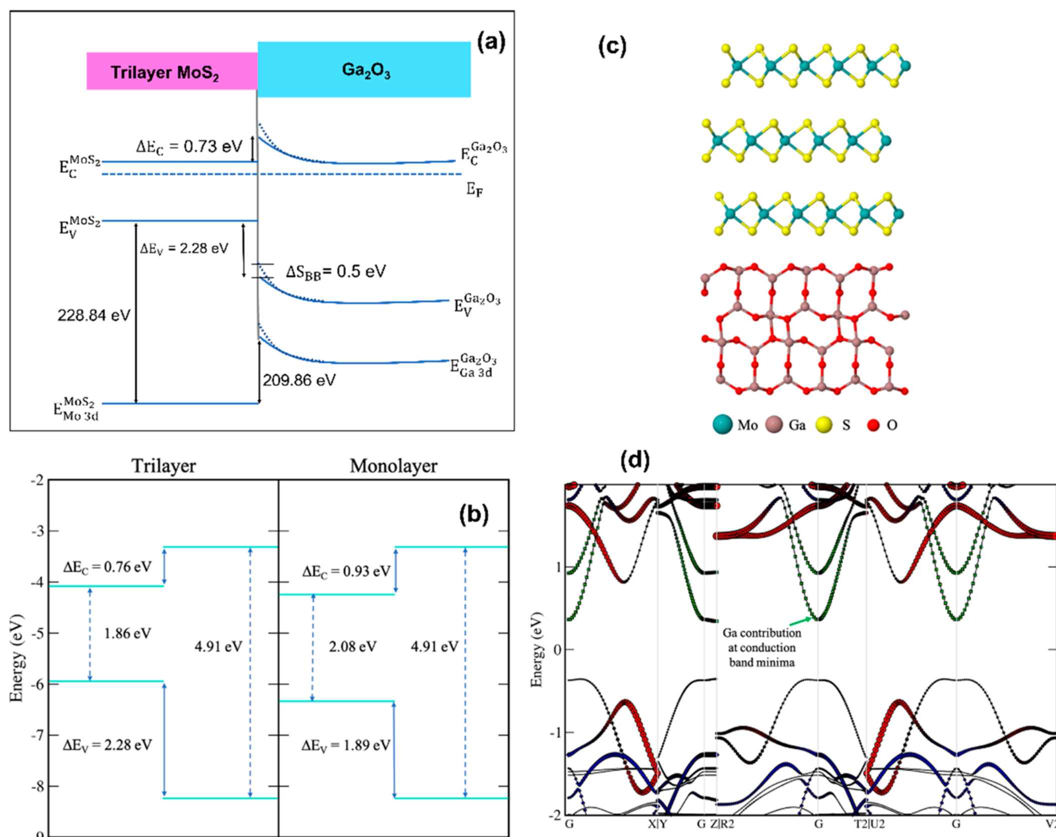

Figure 4. (a) Schematic of an experimental energy band alignment diagram of the 3L MoS_2/β-Ga_2O_3 heterostructure. The dashed and solid lines represent the band banding in β-Ga_2O_3 before and after the heterojunction formation, respectively. (b) Theoretical energy band alignments of 1L and 3L MoS_2/β-Ga_2O_3 heterostructures. (c) Side view of the 3L MoS_2/β-Ga_2O_3 heterostructure. (d) Band structure of the 3L MoS_2/β-Ga_2O_3 heterostructure.

Lorentzian function was used to fit the XPS spectra. Also, the standard C 1s (284.8 eV) was used to calibrate the binding energy (BE)[36] data. The survey scan of β-Ga_2O_3 and MoS_2 is shown in Figure S1. Figure 2a represents the Mo 3d CLs of as-grown 3L MoS_2. The spectra consist of two peaks centered at 229.9 and 233.0 eV, corresponding to $3d_{5/2}$ and $3d_{3/2}$, respectively. Apart from the peaks of Mo 3d, there is a slight hump in the spectra at 227.0 eV that corresponds to S 2s. The spectra of S 2p deconvoluted into two peaks, $2p_{3/2}$ and $2p_{1/2}$, with centers at 162.7 and 163.8 eV[37,38] (Figure 2b). Figure 2c shows the CLs of Ga 3d and O 1s, respectively. The Ga 3d peak was deconvoluted into two peaks, Ga^{2+} and Ga^{3+}, centered at 19.8 and 20.1 eV, respectively. The core-level spectra of O 1s were also deconvoluted into two peaks, O(I) and O(II), at 530.7 and 531.5 eV, respectively (Figure 2d). The lattice oxygen of Ga_2O_3 and oxygen adsorbed at the surface were ascribed to the O(I) and O(II) peaks, respectively.[39]

Figure 3a depicts the XPS spectra of Ga 3d for pristine β-Ga_2O_3 and the MoS_2/β-Ga_2O_3 heterostructure. The Ga 3d peak shifts toward higher BE (~0.5 eV) after MoS_2 transfer on Ga_2O_3. This shift of BE could be due to a different compound formation. However, we do not see any compound of Ga with Mo or S having binding energy values in this range. This suggests no chemical bonding between MoS_2 and β-Ga_2O_3, and it is purely a van der Waals heterojunction. The other possibility of this shift could be a change in band bending caused by charge redistribution at the MoS_2/β-Ga_2O_3 heterointerface, as suggested in refs 40−43. We estimated the surface band bending (SBB) in the pristine β-Ga_2O_3 and after the heterojunction formation. The band bending in pristine β-Ga_2O_3 was estimated by the following equations:

$$\phi_B = E_g^{Ga_2O_3} - (E_{VBM} - E_F) \tag{1}$$

$$SBB = \phi_B - (E_C - E_F)_{Bulk} \tag{2}$$

where ϕ_B is the interface barrier in β-Ga_2O_3 and $(E_{VBM} - E_F)$ is the valence band position from the Fermi level, which was found to be 3.35 eV (Figure 3c). $(E_C - E_F)_{Bulk}$ is the difference between the work function and electron affinity of β-Ga_2O_3. The work function of β-Ga_2O_3 is 4.15 eV calculated by Kelvin probe force microscopy (KPFM) (see Figure S2 of the Supporting Information). The electron affinity of β-Ga_2O_3 is 4.00 eV.[44] The value of SBB in the case of pristine β-Ga_2O_3 was estimated to be 1.2 eV, and it is in the upward direction. When the MoS_2 layer was put on the β-Ga_2O_3, we found an increase in the Ga 3d level energy by 0.5 eV, which resulted in a reduction of band bending at the surface by the same amount. This means that the band bending is reduced to 0.7 eV after the heterojunction formation. A higher positive SBB results in electron depletion, making it difficult to make good ohmic contact on such surfaces. As the band bending decreases, the contact resistance between the metal/MoS_2 will decrease, leading to the increment in current in heterostructure-based devices.

The valence band spectra were used to calculate the valence band maximum (VBM) for MoS_2 and β-Ga_2O_3. According to Figure 3b,c, the VBM for MoS_2 and β-Ga_2O_3 is 1.07 and 3.35

https://doi.org/10.1021/acsaelm.3c00120
ACS Appl. Electron. Mater. XXXX, XXX, XXX−XXX

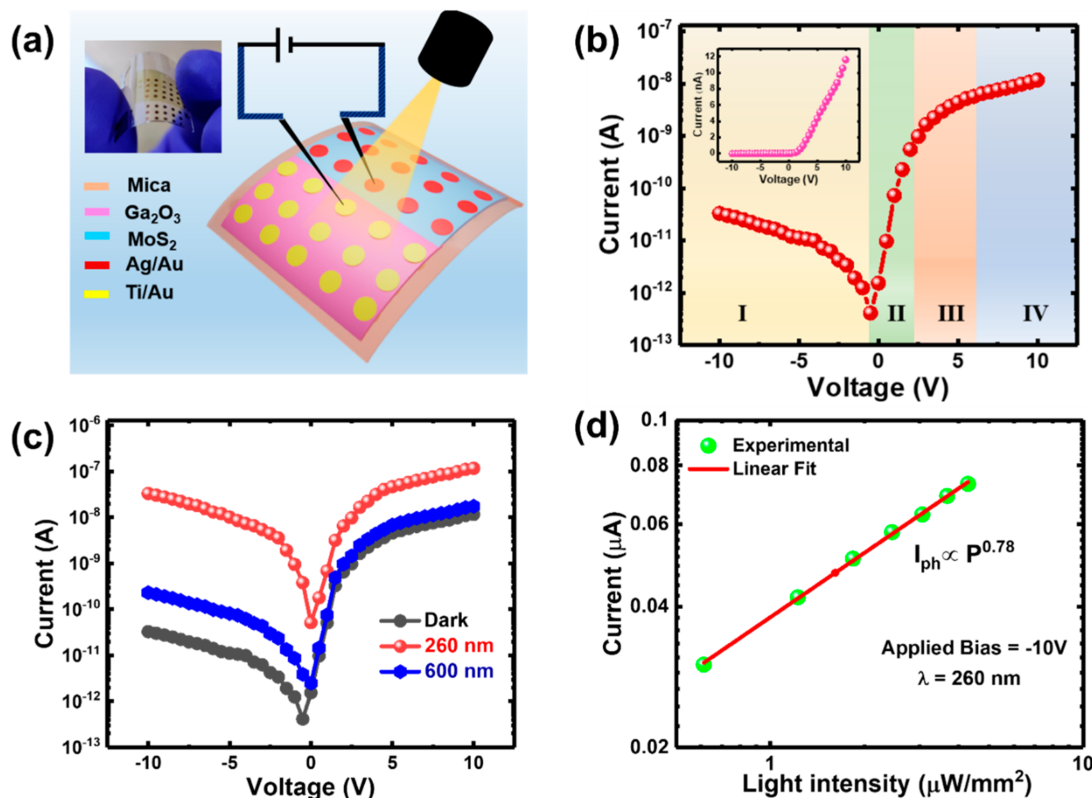

Figure 5. (a) Schematic illustration of the $MoS_2/\beta\text{-}Ga_2O_3$ flexible photodiode. A camera image of the photodiode is shown in the top left corner. (b) Logarithmic and linear (inset) $I-V$ curve of the photodiode without light illumination, showing a good rectification characteristic. (c) $I-V$ measurements of the photodiode with and without light illumination. (d) Logarithmic plot of photocurrent versus light intensity.

eV, respectively. The VBO (ΔE_V) and CBO (ΔE_C) for the $MoS_2/\beta\text{-}Ga_2O_3$ heterojunction were estimated using Kraut's approach[45] using the following equations:

$$\Delta E_V = (E_{Mo3d} - E_{VBM})_{MoS_2} - (E_{Ga3d} - E_{VBM})_{Ga_2O_3} - (E_{CL}^{MoS_2} - E_{CL}^{Ga_2O_3}) \quad (3)$$

$$\Delta E_C = E_g^{Ga_2O_3} - E_g^{MoS_2} - \Delta E_V \quad (4)$$

where $E_{Mo\ 3d}$ and $E_{Ga\ 3d}$ are the binding energies of Mo 3d and Ga 3d core levels, respectively. E_{VBM} is the valence band maxima corresponding to MoS_2 and $\beta\text{-}Ga_2O_3$. $E_{CL}^{MoS_2}$ and $E_{CL}^{Ga_2O_3}$ are the core-level energies of MoS_2 and $\beta\text{-}Ga_2O_3$, respectively. $E_g^{Ga_2O_3}$ and $E_g^{MoS_2}$ are the bandgaps of Ga_2O_3 and MoS_2, respectively. The bandgaps of $\beta\text{-}Ga_2O_3$ (4.71 eV) and MoS_2 (1.70 eV) were determined using UV−vis spectroscopy, as described in Figure S3 of the Supporting Information. By combining the measured values of various levels, a band alignment diagram of the $MoS_2/\beta\text{-}Ga_2O_3$ heterostructure is derived (Figure 4a). Valence band offset (ΔE_V) and conduction band offset (ΔE_C) were found to be 2.28 and 0.73 eV, respectively.

Furthermore, we performed first-principles calculations to analyze our experimental findings of the $MoS_2/\beta\text{-}Ga_2O_3$ heterostructure. The $1 \times \sqrt{3}$ supercell of monolayer (1L) and trilayer MoS_2 is modeled with a 1 × 1 supercell of $\beta\text{-}Ga_2O_3$ (100) along with the vacuum of 30 Å to form heterostructures. The bandgaps of 1L MoS_2, 3L MoS_2, and $\beta\text{-}Ga_2O_3$ are calculated to be 2.08, 1.86, and 4.91 eV, respectively. Initially, the band edge alignment is obtained by observing type I straddling alignment (see Figure 4b). The MoS_2 monolayer ($a = b = 3.16$ Å) is strained in the heterostructure due to lattice mismatch. The heterostructure and the corresponding band structure can be observed in Figure 4c and d. The corresponding high-symmetry path is obtained from SeeK-path.[46] We see a Ga contribution at the conduction band minima of the heterostructure. This is in sync with the observations of Huan et al.[32] The electron motion toward the minimum band edge facilitates the band bending and, hence, the Ga contribution. The valence band offsets (ΔE_V) for the corresponding IL and 3L heterostructures are 1.89 and 2.28 eV. The corresponding conduction band offsets (ΔE_C) are 0.93 and 0.76 eV, respectively. For 3L $MoS_2/\beta\text{-}Ga_2O_3$, the obtained ΔE_V and ΔE_C are in good agreement with our experimental results. The band offsets are the driving force behind the spatial separation of the electrons and holes, whereby a lower band offset supports more charge transfer.

2.2. Flexible $MoS_2/\beta\text{-}Ga_2O_3$ Photodiode.

Figure 5a shows the schematic illustration of the $MoS_2/\beta\text{-}Ga_2O_3$ heterojunction photodiode fabricated on a muscovite mica substrate. Muscovite mica outperforms traditional flexible substrates due to its atomically smooth surface, exceptional flexibility, and high-temperature durability. To improve the junction quality and obtain stable contacts, the as-fabricated device was annealed at 300 °C for 1 h under Ar atmosphere protection. Figure 5b depicts the current−voltage ($I-V$) curve of the device in the dark with an active device area (A) of 1.3 mm^2. From the asymmetric nature of the $I-V$ curve, an excellent rectification characteristic over 5×10^2 was obtained between ±10 V, revealing the junction formation between MoS_2 and $\beta\text{-}Ga_2O_3$. The ohmic nature of $I-V$ curves on Ga_2O_3 and MoS_2 also conformed to the junction formation (shown in

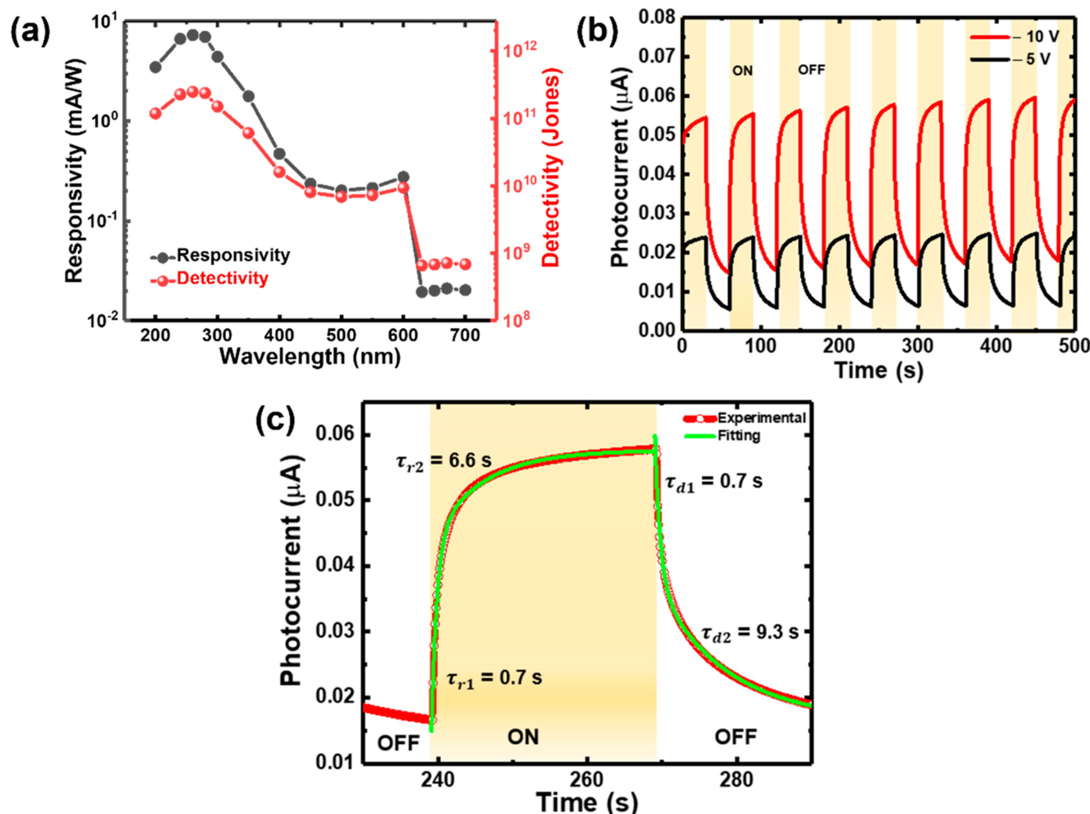

Figure 6. (a) Responsivity and detectivity of the MoS_2/β-Ga_2O_3 flexible photodiode as a function of incident light wavelength. (b) Time-resolved photoresponse of the device illuminated with 260 nm light at −5 V and −10 V biasing voltages. (c) Rise and decay time of the photodiode at −10 V. The graph has been fitted with the biexponential equation.

Supporting Information Figure S4). Moreover, four typical regions of the diode are shown: (I) reverse bias region, (II) linear diode region, (III) current injection region, and (IV) series resistance dominant region. The dark current of the device was fitted with the following diode equation:[47]

$$I = I_s\left[\exp\left(\frac{eV}{nk_BT}\right) - 1\right] \tag{5}$$

where I_s and n are the dark saturation current and ideality factor of the diode, respectively. The ideality factor was calculated to be ∼9.87. The high value of n in comparison to the ideal value ($1 \leq n \leq 2$) indicates the presence of defects at the surface and interface between MoS_2 and β-Ga_2O_3. Further, the device was illuminated with various wavelengths to check the photoresponse.

Since the MoS_2 and Ga_2O_3 possess different bandgaps, photogenerated charge carriers are generated under both visible to ultraviolet (UV) irradiation. Figure 5c clearly shows that the MoS_2/β-Ga_2O_3 photodiode has a good photoresponse to visible and UV light. We observed that the change in current in the reverse bias is more noticeable than in the forward bias. In reverse bias, the PDCR was found to be 10 and 10^3 in the visible (600 nm wavelength) and UV region (260 nm wavelength), respectively. It is worth noting that the PDCR of 10^3 was obtained at a low power density (21.1 μW/mm^2), and it will increase as the power density increases. At a wavelength of 260 nm, the variation of photocurrent (I_p) of the device with power density was plotted in Figure 5d, which was fitted with the power law $I_p = \alpha P\lambda^{\beta}$, where α is a proportionality constant, P_λ is power density, and β is an empirical constant that determines the photocurrent response with power density. The value of β was deduced to be 0.78 (<1), indicating the presence of carrier trap states located between the conduction band and Fermi level.[48] The critical parameters for evaluating the performance of a photodiode are responsivity (R_λ) and detectivity (D^*), which are defined as[49]

$$R_\lambda = \frac{I_p - I_d}{P_\lambda A_c} \tag{6}$$

$$D^* = \sqrt{\frac{A_c}{2eI_d}} \cdot R_\lambda \tag{7}$$

where I_d is the dark current of the photodiode. As shown in Figure 6a, the responsivity was measured at −10 V biased voltage with varying wavelengths. The value of R_λ increases with a decrease in wavelength. In the visible region, the R_λ was found to be 21 μA/W at a wavelength of 600 nm, corresponding to the bandgap of MoS_2. We achieved a maximum responsivity of 7.21 mA/W at a wavelength of 260 nm (UV region), corresponding to the bandgap of β-Ga_2O_3. The obtained responsivity is higher than the previously reported responsivity of the MoS_2/β-Ga_2O_3 photodiode.[31] Furthermore, the detectivity was calculated to determine the signal-detecting ability of the photodiode. Under UV illumination, the detectivity was calculated as 2.4×10^{11} Jones. Further, we obtained a time-resolved photoresponse by periodically switching a 260 nm UV signal on and off at −5 V and −10 V biasing voltages to evaluate the response speed of the photodiode. The on/off levels remain steady throughout

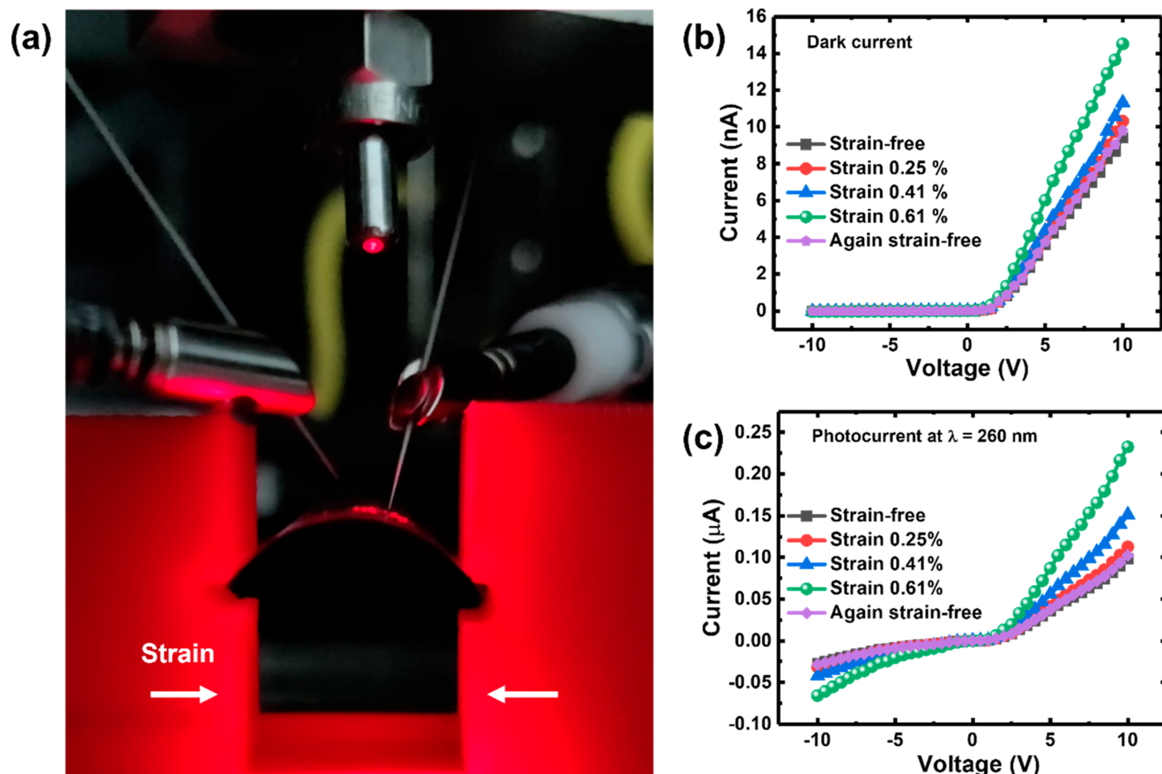

Figure 7. (a) Camera image of the flexible photodiode with tensile strain. Variation of (b) dark current and (c) photocurrent under different tensile strains.

time, as shown in Figure 6b, demonstrating the excellent repeatability and reliability of the device in terms of photoswitching behavior. The fast and slow components of the rise and decay time were calculated by fitting the experimental data with the following equation:[50]

$$I(t) = I_0 + C_1 e^{-(t-t_0)/\tau_1} + C_2 e^{-(t-t_0)/\tau_2} \quad (8)$$

where $I(t)$ and I_0 are the current at any time t and steady-state current, respectively. τ_1 and τ_2 are relaxation time constants, whereas C_1 and C_2 are fitting constants. τ_{r1} (τ_{r2}) and τ_{d1} (τ_{d2}) denote the fast (slow) components of the rise time and decay time, respectively. τ_{r1} (τ_{r2}) and τ_{d1} (τ_{d2}) are found to be 0.7 s (6.6 s) and 0.7 s (9.3 s), respectively (see Figure 6c). The rise and decay time show the slow photoresponse time of the device. The slow response of the device may be attributed to the presence of structural defects and vacancies in pulsed laser deposition (PLD)-grown Ga_2O_3 and chemical vapor deposition (CVD)-grown MoS_2. B. R. Tak et al.[39] demonstrated the existence of oxygen and gallium vacancy defects in Ga_2O_3. Additionally, large-area MoS_2 films synthesized by CVD may have defects (mainly S vacancies), grain boundaries, adlayers, and disordered crystal orientations.[51] Defects can critically influence the electrical properties of the device.

Figure 7a shows the camera image of the flexible MoS_2/β-Ga_2O_3 photodiode under uniaxial tensile strain. Using a homemade bending system, the tensile strain was applied to the device by bending the muscovite mica substrate. We studied the functionalities of the device by bending the muscovite mica substrate with various bending radii and bending cycles (Figure 8a). The equation $\epsilon = \frac{t_s + t_f}{2R}$ was used to calculate the tensile strain in the device, where t_s and t_f are the thickness of the mica substrate (86.41 μm) and the thickness of the film, respectively. The thickness of the film includes the thickness of β-Ga_2O_3 (0.23 μm) and the thickness of MoS_2 (2 nm). R represents the radius of curvature. The calculated strain values for the various radius of curvature are shown in Table 1.

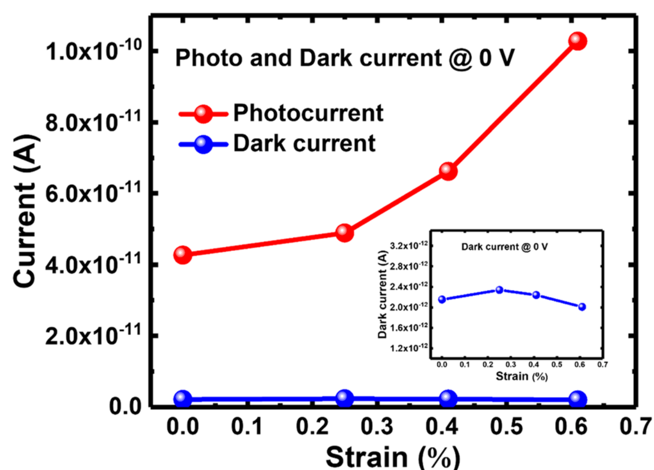

Figure 8. Variation in the photocurrent and dark current with strain at zero bias voltage. The inset shows the variation of the dark current.

Prior to exploring the influence of strain on the photodetection of the MoS_2/β-Ga_2O_3 flexible photodiode, we have evaluated the electrical transport of the device under tensile strain without optical illumination. Under 10 V bias, the dark current increases from 9.2 nA to 15.1 nA as the tensile strain increases from 0% to 0.61%, as shown in Figure 7b.

The increment in the dark current and photocurrent can be explained by the piezoelectric and piezo-phototronic effects. It

https://doi.org/10.1021/acsaelm.3c00120
ACS Appl. Electron. Mater. XXXX, XXX, XXX−XXX

Table 1. Change in Dark Current, Photocurrent, and Responsivity under Different Strain States

bending state	radius of curvature (mm)	strain (%)	increase in dark current (%)	increase in photocurrent (%)	relative responsivity (%)
Flat	∞	0	0	0	0
state 1	16.9	0.25	9	44	14
state 2	10.6	0.41	20	93	53
state 3	6.7	0.61	60	155	136
again flat	∞	0	4	2	3

has been reported that the MoS_2 with the odd number of layers produces in-plane piezoelectric polarization charges under external strain due to the lack of inversion symmetry/centrosymmetry.[52] When we applied the tensile strain, positive polarization charges were generated at the heterojunction interface due to the piezoelectric effect, resulting in a positive piezo potential within the MoS_2. The induced positive piezo-potential attracts the free electrons of MoS_2 toward the MoS_2/β-Ga_2O_3 interface, lowering the interface barrier. The electrical properties of any device are highly sensitive to changes in interface barrier. An increase in interface barrier leads to a decrease in dark current and vice versa. The interface barrier decreases in our case, resulting in an increase in dark current. The reduction in interface barrier with increasing tensile strain has been experimentally verified. The interface barrier (ϕ_B) is calculated by standard thermionic emission theory.[53]

$$\phi_B = \frac{kT}{e}\ln\left(\frac{AA^*T^2}{I_s}\right) \quad (9)$$

where A and A^* are the effective area of the device and effective Richardson constant, respectively. I_s is saturation current calculated from the I−V curve. We calculated that the interface barrier under strain-free condition is 0.97 eV, which decreases to 0.92 eV at 0.61% strain. We measured the dark current for three values of applied strain and found that the

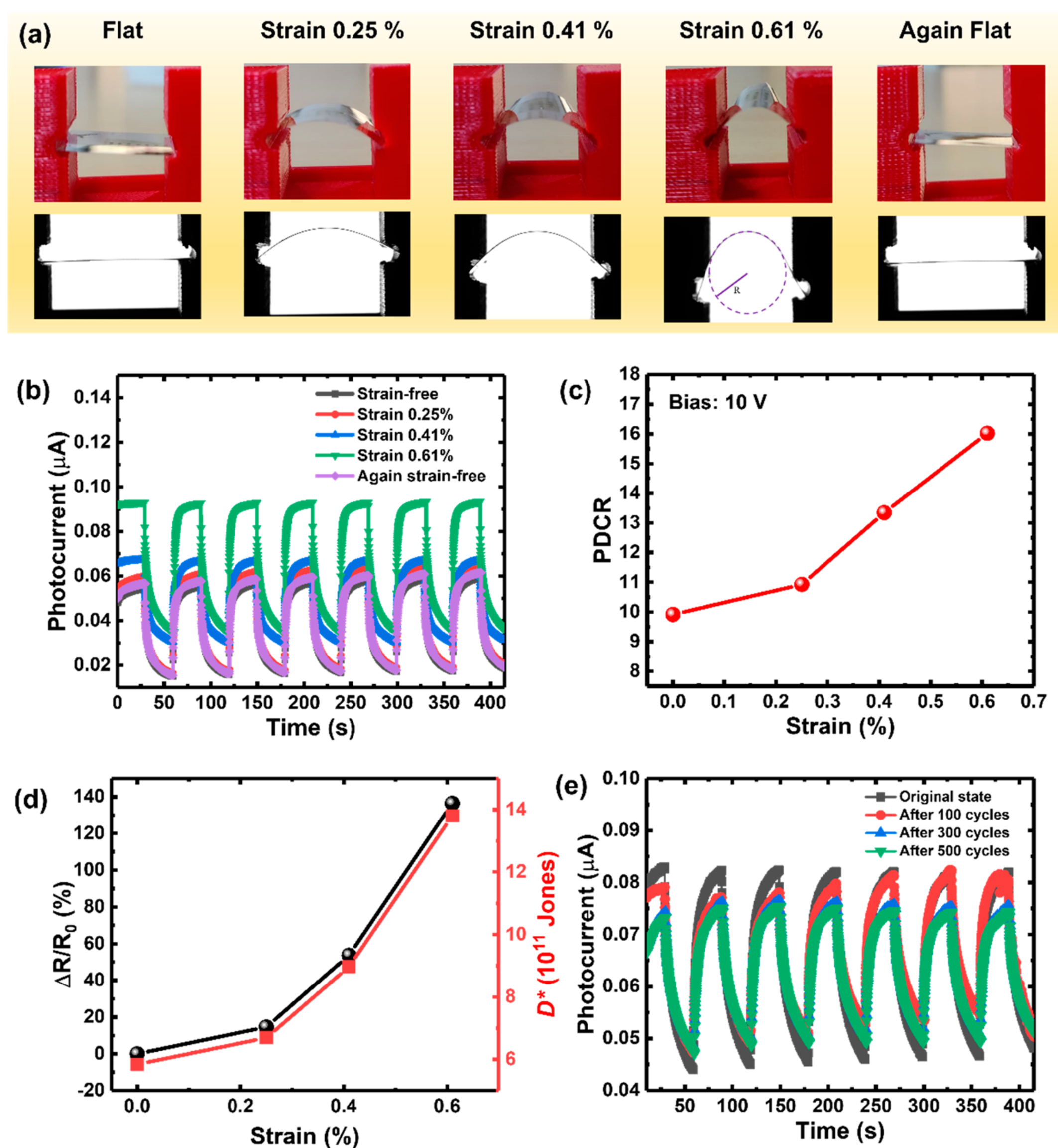

Figure 9. (a) Camera images (red) and CCD camera images (black) of a flexible photodiode under different strain states. (b) Time-dependent photoresponse of the device under different bending states (strain states). Strain dependence of the (c) PDCR and (d) relative responsivity and detectivity at 10 V bias. (e) Time-dependent photoresponse of the device under different bending cycles.

https://doi.org/10.1021/acsaelm.3c00120
ACS Appl. Electron. Mater. XXXX, XXX, XXX−XXX

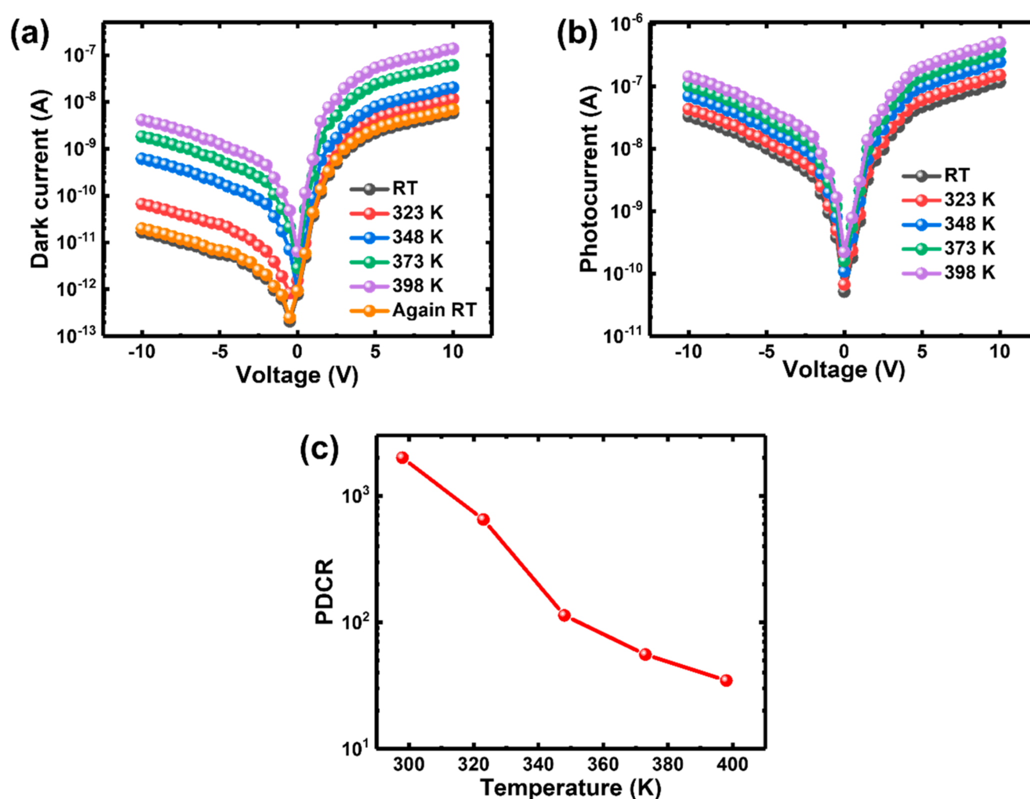

Figure 10. Variation of (a) dark current and (b) photocurrent with temperature. (c) Temperature-dependent PDCR of the photodiode.

dark current increases monotonically with the increase in the strain value.

We also performed Raman measurements on the MoS_2 film with applied strain (Figure S5a) and found that the increase in strain results in a blue shift of the Raman E^1_{2g} line. This shows that the film is subjected to tensile strain and that the strain increases as the bending radius decreases. One of the consequences of tensile strain is the reduction in the bandgap.[54] We found from the first-principles calculations that the bandgap of 3L MoS_2 decreases with increasing tensile strain (Figure S5b). It is well known that the reduction in bandgap also decreases the interface barrier, resulting in an increase in dark current.

We observed an increase in photocurrent with increasing tensile strain. At a wavelength of 260 nm, power density of 4.3 $\mu W/mm^2$, and voltage of 10 V, the photocurrent increases from 09 μA to 0.23 μA as the tensile strain increases from 0% to 0.61% (Figure 7c). The photocurrent and dark current of the device were measured at zero bias voltage to establish that the increase in photocurrent is solely due to tensile strain. As illustrated in Figure 8, the photocurrent increases with increasing strain, whereas the dark current does not. This is because the induced positive polarization charges at the interface widened the depletion region, providing an additional driving force to separate photogenerated electrons and holes more effectively. The expanded depletion region also reduces the recombination of photogenerated electron−hole pairs, accelerating charge carrier transport across the junction and increasing photocurrent.[55] We recorded the time-dependent photoresponse of the photodiode under various tensile strain states. As shown in Figure 9b, the photocurrent increases with tensile strain. Also, the photodiode showed excellent stability over a long period of time for a particular value of strain. We calculated the PDCR, relative responsivity ($\Delta R/R_0$), and detectivity (D^*) of the device subjected to different tensile strain states. R_0 is defined as the responsivity under the flat (strain-free) state. As shown in Figure 9c,d, the PDCR and $\Delta R/R_0$ showed a similar trend to photocurrent with strain (see Figure S7 in the Supporting Information for the trend of photocurrent). At the maximum strain of 0.61% and illumination at 260 nm, the PDCR and $\Delta R/R_0$ were found to be 16 and 136%. The highest value of detectivity was found to be 3.27×10^{11} Jones at 0.61% strain. As stated above, the reduction in interface barrier and change in the depletion region width as a result of applied strain are responsible for the increase in PDCR, $\Delta R/R_0$, and detectivity of our device.

The service life of a flexible device is determined not only by its capacity to retain the photoelectric response but also by its robustness in the face of performance loss induced by bending. To test the bending stability of the photodiode, we measured the time-resolved photoresponse of the device at 10 V bias voltage and 260 nm illumination wavelength after 0, 100, 300, and 500 bending cycles. The photodiode was subjected to a maximum tensile strain of 0.61% during all of the bending cycles. From Figure 9e, we observed that the photocurrent was almost constant for 100 bending cycles. A slight decrement in the photocurrent was observed after 300 bending cycles; later, it became constant. Even after 500 bending cycles, the photodiode showed only a 7% reduction in photocurrent, confirming the excellent bending durability and robustness of the photodiode. The deteriorated electrical connections between the MoS_2, Ga_2O_3 films, and electrodes might cause a minor change in photoresponse.[56,57]

We also explored the high-temperature performance of the $MoS_2/\beta\text{-}Ga_2O_3$ flexible photodiode. Figure 10a,b shows the variation of dark and photocurrent with temperature. We

https://doi.org/10.1021/acsaelm.3c00120
ACS Appl. Electron. Mater. XXXX, XXX, XXX−XXX

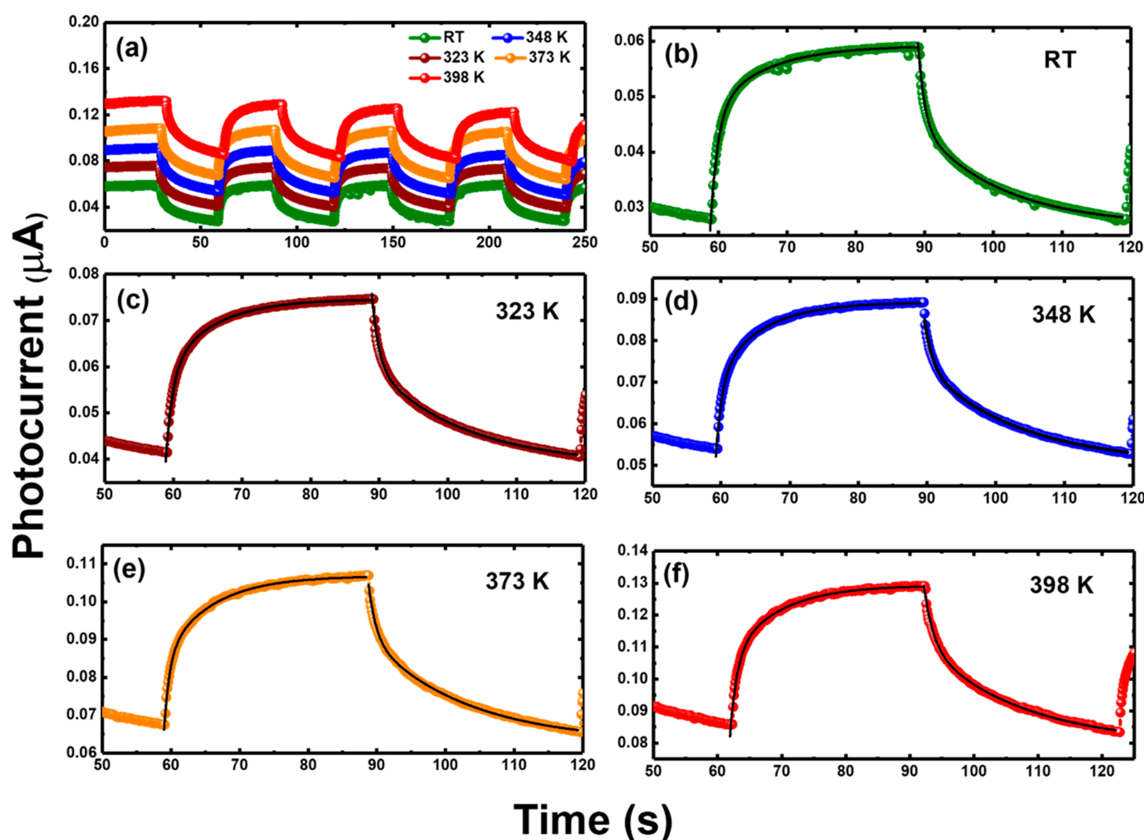

Figure 11. (a) Time-resolved photoresponse of the photodiode at different temperatures. (b−f) Time-resolved photoresponse for different temperatures fitted with the biexponential equation.

observed that both dark current and photocurrent increased with an increase in temperature. However, the dark current increased faster than the photocurrent due to the thermally generated charge carriers. As a result, the PDCR of the device decreases with rising temperature (Figure 10c). When the temperature was raised from RT to 398 K, the PDCR was reduced from 2000 to 34 at −10 V bias. The RT dark current level was again achieved when the device was cooled down from high temperature to RT, showing the excellent thermal stability of the device (Figure 10a). We performed high-temperature measurements only up to 125 °C due to the system limitations. However, the photodiode can perform at temperatures higher than 125 °C also.

We also obtained the time-resolved photoresponse of the device by periodically switching a 260 nm UV signal on and off at −10 V biasing voltage from RT to 398 K. As shown in Figure 11a, the on/off levels remain steady over time, showing the excellent repeatability and reliability of the device in terms of photoswitching behavior even at high temperatures. The time-resolved photoresponse at different temperatures was then fitted with the biexponential eq 8 to calculate the change in rise and decay times with temperature (Figure 11b−f). The variation in the rise and decay times with temperature is shown in Table 2. It has been observed that fast/slow (τ_{r1}/τ_{r2}) rise time components did not show any significant variation with temperature. However, fast/slow (τ_{d1}/τ_{d2}) decay time components increase with increasing temperature.

3. CONCLUSIONS

In conclusion, we fabricated a MoS_2/β-Ga_2O_3 van der Waals heterojunction to explore the new dimensions of the 2D TMDC materials. We proposed a band diagram model for the MoS_2/β-Ga_2O_3 heterostructure based on our experimental findings. This model shows a type I band alignment configuration with valence band offsets of 2.28 eV and conduction band offsets of 0.73 eV, which agrees with the first-principles calculations of VBO and CBO. We then fabricated a MoS_2/β-Ga_2O_3 flexible photodiode on the flexible and transparent mica substrate and investigated the impact of bending/tensile strain. The PDCR, responsivity, and detectivity of the device were calculated to be 10^3, 7.21 mA/W, and 2.4 $\times$ 10^{11} Jones, respectively. We observed an enhancement of 155% and 136% in the photocurrent and responsivity of the device under 0.61% tensile strain due to the piezoelectric and piezo-phototronic effects. Furthermore, no significant change in device performance was observed even after 500 bending cycles at a maximum 0.61% strain, demonstrating the excellent flexibility and robustness of the photodiode. The device can be used as a high-temperature photodiode due to its excellent thermal stability at high temperatures. The findings of this

Table 2. Variation in the Rise and Decay Times with Temperature

	rise time (s)		decay time (s)	
temperature (K)	τ_{r1}	τ_{r2}	τ_{d1}	τ_{d2}
RT	1.08	7.82	0.82	11.52
323	1.01	6.82	0.85	12.51
348	0.90	6.54	1.00	13.86
373	0.81	6.92	1.40	15.73
398	1.08	7.49	2.14	18.71

https://doi.org/10.1021/acsaelm.3c00120
ACS Appl. Electron. Mater. XXXX, XXX, XXX−XXX

study open up a pathway toward heterostructure-based flexible electronics.

4. EXPERIMENTAL SECTION

4.1. Heterostructure Formation. For band alignment studies, we have taken a free-standing n-type β-Ga_2O_3 (10 × 10 mm) sample of thickness 0.68 mm, with (−201) orientation. The large-area (centimeter-scale) MoS_2 film was grown on a SiO_2/Si substrate by CVD (see ref 58). The MoS_2 film was transferred onto the β-Ga_2O_3 sample via a quasi-dry layer transfer process. The samples were characterized by Raman spectroscopy, XPS, atomic force microscopy (AFM), UV−vis, and KPFM). The Raman measurements were carried out at room temperature (RT) using a Horiba Scientific (LabRAM HR Evolution) with a 514 nm laser. A monochromatic Al Kα X-ray line (probe size ∼1.7 mm × 2.7 mm, energy 1486.7 eV) was used for XPS analysis. A Philips X-pert Pro system with Cu Kα (λ = 1.54 Å) was used to perform the XRD. An FESEM-Zeiss microscope (backscattering mode) was used to perform FESEM.

4.2. Flexible Photodiode Fabrication. To fabricate the flexible MoS_2/β-Ga_2O_3 photodiode, the gallium oxide (Ga_2O_3) film was deposited epitaxially on the muscovite mica substrate using the PLD technique. During the growth, the temperature and oxygen pressure were 600 °C and 5×10^{-2} Torr, respectively. The complete growth process was explained in ref 59. After the growth, MoS_2 was transferred onto the β-Ga_2O_3/mica substrate by the quasi-dry layer transfer process. The ohmic contacts of Ag/Au (20/60 nm) and Ti/Au (20/60 nm) were deposited on MoS_2 and Ga_2O_3, respectively, by e-beam evaporation using a metal shadow mask. The photocurrent measurements were performed using a DC probe station (Ever-BeingEB6) coupled with a semiconductor characterization system from Keithley (SCS4200). A xenon lamp (75 W) was used to measure the photoresponse of the device, which was combined with a computer-interfaced monochromator (Bentham TMC-300 V). A Thorlabs power meter (PM-100D) was used for the power spectrum of the xenon lamp.

4.3. Quasi-Dry Layer Transfer Process. In the typical transfer process, polydimethylsiloxane (PDMS) film was first attached to the as-grown MoS_2 film, and the PDMS/MoS_2/growth substrate assembly was then soaked with DI water. The PDMS/MoS_2 stack was mechanically peeled off from the growth substrate. The Na_2S/Na_2SO_4 layer below the MoS_2 layer was dissolved in the water and used the buoyancy force to support the PDMS/MoS_2 stack mechanically. To prevent water trapping between MoS_2 and the target substrate, the PDMS/MoS_2 stack was dried using N_2 gas before being transferred onto the target substrate. By heating the PDMS/MoS_2/target substrate assembly at 140 °C on a hot plate, the PDMS film was separated from the surface of the MoS_2 film. Because of the heating, the PDMS lost its adhesion to the MoS_2 and readily peeled off from the target substrate. The detailed transfer process has been discussed in ref 60.

4.4. Computational Methodology. The Vienna ab initio simulation package (VASP) with projected augmented wave (PAW) potential is implemented for first-principles-based calculations under the framework of density functional theory (DFT).[61−63] The generalized gradient approximation (GGA) is employed for the exchange−correlation interaction of electrons by the functional proposed by Perdew, Burke, and Ernzerhof (PBE).[64] The energy cutoff was 500 eV, the tolerance energy was 0.001 meV, and ionic force tolerance was 0.01 eV/Å using conjugate gradient minimization. The energetics is also obtained by the HSE06 (Heyd−Scuseria−Ernzerhof) functional.[65] The van der Waals correction is incorporated by the Tkatchenko−Scheffler scheme.[66]

■ ASSOCIATED CONTENT

Supporting Information

The Supporting Information is available free of charge at https://pubs.acs.org/doi/10.1021/acsaelm.3c00120.

XPS and KPFM measurements of β-Ga_2O_3 and MoS_2, Tauc−Mott plot for bandgap, bandgap vs tensile strain plot for MoS_2, photoresponse of the MoS_2/β-Ga_2O_3 photodiode under different strain states (PDF)

■ AUTHOR INFORMATION

Corresponding Author

Rajendra Singh − *Department of Physics, Indian Institute of Technology Delhi, New Delhi 110016, India; Department of Electrical Engineering and Nanoscale Research Facility, Indian Institute of Technology Delhi, New Delhi 110016, India;* orcid.org/0000-0002-6890-6904; Email: rsingh@physics.iitd.ac.in

Authors

Madan Sharma − *Department of Physics, Indian Institute of Technology Delhi, New Delhi 110016, India;* orcid.org/0000-0001-5274-9580

Arunima Singh − *Department of Physics, Indian Institute of Technology Delhi, New Delhi 110016, India;* orcid.org/0000-0002-7344-9816

Ashok Kapoor − *Department of Physics, Indian Institute of Technology Delhi, New Delhi 110016, India*

Aditya Singh − *Department of Physics, Indian Institute of Technology Delhi, New Delhi 110016, India;* orcid.org/0000-0002-4301-1397

Bhera Ram Tak − *Department of Physics, Indian Institute of Technology Delhi, New Delhi 110016, India;* orcid.org/0000-0002-6150-9180

Shuchi Kaushik − *Department of Physics, Indian Institute of Technology Delhi, New Delhi 110016, India;* orcid.org/0000-0002-1927-7945

Saswata Bhattacharya − *Department of Physics, Indian Institute of Technology Delhi, New Delhi 110016, India;* orcid.org/0000-0002-4145-4899

Complete contact information is available at: https://pubs.acs.org/10.1021/acsaelm.3c00120

Notes

The authors declare no competing financial interest.

■ ACKNOWLEDGMENTS

M. Sharma thanks the Department of Science & Technology (DST) for the award of the research fellowship. A. Singh acknowledges IIT Delhi for the senior research fellowship. S. Bhattacharya acknowledges the financial support of SERB under the Core Research Grant [CRG/2019/000647]. We acknowledge the High-Performance Computing (HPC) and Veena Cluster facility at IIT Delhi for computational resources. The authors acknowledge the Nanoscale Research Facility (NRF) and Central Research Facility (CRF), Indian Institute of Technology Delhi, New Delhi, for providing the characterization facilities. We would also like to acknowledge Grand Challenge Project on MBE growth of 2D materials sponsored by Ministry of Human Resource Development (MHRD), India, and IIT Delhi for partial financial support for this work.

■ REFERENCES

(1) Lee, Y.; Myoung, J.; Cho, S.; Park, J.; Kim, J.; Lee, H.; Lee, Y.; Lee, S.; Baig, C.; Ko, H. J. Bioinspired gradient conductivity and stiffness for ultrasensitive electronic skins. *ACS Nano* **2021**, *15* (1), 1795−1804.

(2) Bandodkar, A. J.; Jeang, W. J.; Ghaffari, R.; Rogers, J. A. Wearable sensors for biochemical sweat analysis. *Annual Review of Analytical Chemistry* **2019**, *12*, 1−22.
(3) Lee, S.-K.; Kim, B. J.; Jang, H.; Yoon, S. C.; Lee, C.; Hong, B. H.; Rogers, J. A.; Cho, J. H.; Ahn, J.-H. J. Stretchable graphene transistors with printed dielectrics and gate electrodes. *Nano Lett.* **2011**, *11* (11), 4642−4646.
(4) Korn, T.; Heydrich, S.; Hirmer, M.; Schmutzler, J.; Schüller, C. J. A. P. L. Low-temperature photocarrier dynamics in monolayer MoS2. *Appl. Phys. Lett.* **2011**, *99* (10), 102109.
(5) Splendiani, A.; Sun, L.; Zhang, Y.; Li, T.; Kim, J.; Chim, C.-Y.; Galli, G.; Wang, F. J. N. l. Emerging photoluminescence in monolayer MoS2. *Nano Lett.* **2010**, *10* (4), 1271−1275.
(6) Yim, C.; O'Brien, M.; McEvoy, N.; Winters, S.; Mirza, I.; Lunney, J. G.; Duesberg, G. S. J. Investigation of the optical properties of MoS2 thin films using spectroscopic ellipsometry. *Appl. Phys. Lett.* **2014**, *104* (10), 103114.
(7) Sweet, C.; Pramanik, A.; Jones, S.; Ray, P. C. J. A. o. Two-photon fluorescent molybdenum disulfide dots for targeted prostate cancer imaging in the biological II window. *ACS omega* **2017**, *2* (5), 1826−1835.
(8) Tsai, D.-S.; Liu, K.-K.; Lien, D.-H.; Tsai, M.-L.; Kang, C.-F.; Lin, C.-A.; Li, L.-J.; He, J.-H. J. A. N. Few-layer MoS2 with high broadband photogain and fast optical switching for use in harsh environments. *ACS Nano* **2013**, *7* (5), 3905−3911.
(9) Liu, W.; Kang, J.; Cao, W.; Sarkar, D.; Khatami, Y.; Jena, D.; Banerjee, K. In *High-performance few-layer-MoS 2 field-effect-transistor with record low contact-resistance*; 2013 IEEE international electron devices meeting, IEEE, 2013; pp 19.4.1−19.4.4.
(10) Choi, W.; Cho, M. Y.; Konar, A.; Lee, J. H.; Cha, G. B.; Hong, S. C.; Kim, S.; Kim, J.; Jena, D.; Joo, J. J. A. m. High-detectivity multilayer MoS2 phototransistors with spectral response from ultraviolet to infrared. *Advanced materials* **2012**, *24* (43), 5832−5836.
(11) Tsai, M.-Y.; Tarasov, A.; Hesabi, Z. R.; Taghinejad, H.; Campbell, P. M.; Joiner, C. A.; Adibi, A.; Vogel, E. M. Flexible MoS2 Field-Effect Transistors for Gate-Tunable Piezoresistive Strain Sensors. *ACS Appl. Mater. Interfaces* **2015**, *7* (23), 12850−12855.
(12) Pu, J.; Yomogida, Y.; Liu, K.-K.; Li, L.-J.; Iwasa, Y.; Takenobu, T. Highly Flexible MoS2 Thin-Film Transistors with Ion Gel Dielectrics. *Nano Lett.* **2012**, *12* (8), 4013−4017.
(13) Wu, W.; Wang, L.; Li, Y.; Zhang, F.; Lin, L.; Niu, S.; Chenet, D.; Zhang, X.; Hao, Y.; Heinz, T. F.; Hone, J.; Wang, Z. L. Piezoelectricity of single-atomic-layer MoS2 for energy conversion and piezotronics. *Nature* **2014**, *514* (7523), 470−474.
(14) Zhu, H.; Wang, Y.; Xiao, J.; Liu, M.; Xiong, S.; Wong, Z. J.; Ye, Z.; Ye, Y.; Yin, X.; Zhang, X. Observation of piezoelectricity in free-standing monolayer MoS2. *Nat. Nanotechnol.* **2015**, *10* (2), 151−155.
(15) Wu, W.; Wang, Z. L. Piezotronics and piezo-phototronics for adaptive electronics and optoelectronics. *Nature Reviews Materials* **2016**, *1* (7), 16031.
(16) Wu, W.; Wang, L.; Yu, R.; Liu, Y.; Wei, S.-H.; Hone, J.; Wang, Z. L. Piezophototronic Effect in Single-Atomic-Layer MoS2 for Strain-Gated Flexible Optoelectronics. *Adv. Mater.* **2016**, *28* (38), 8463−8468.
(17) Peng, M.; Li, Z.; Liu, C.; Zheng, Q.; Shi, X.; Song, M.; Zhang, Y.; Du, S.; Zhai, J.; Wang, Z. L. High-Resolution Dynamic Pressure Sensor Array Based on Piezo-phototronic Effect Tuned Photoluminescence Imaging. *ACS Nano* **2015**, *9* (3), 3143−3150.
(18) Guo, P.; Jia, M.; Guo, D.; Wang, Z. L.; Zhai, J. Retina-inspired in-sensor broadband image preprocessing for accurate recognition via the flexophototronic effect. *Matter* **2023**, *6* (2), 537−553.
(19) Guo, P.; Jia, M.; Guo, D.; Wang, W.; Zhang, Y.; Ren, L.; Yu, A.; Wang, Z. L.; Zhai, J. Mechanical Modulation of 2D Electronic Devices at Atto-Joule Energy via Flexotronic Effect. *Adv. Funct. Mater.* **2022**, *32* (34), 2202779.
(20) Xue, F.; Yang, L.; Chen, M.; Chen, J.; Yang, X.; Wang, L.; Chen, L.; Pan, C.; Wang, Z. L. J. N. A. M. Enhanced photoresponsivity of the MoS2-GaN heterojunction diode via the piezo-phototronic effect. *NPG Asia Materials* **2017**, *9* (8), e418−e418.
(21) Jariwala, D.; Marks, T. J.; Hersam, M. C. J. Mixed-dimensional van der Waals heterostructures. *Nature Materials* **2017**, *16* (2), 170−181.
(22) Li, P.; Yuan, K.; Lin, D.-Y.; Xu, X.; Wang, Y.; Wan, Y.; Yu, H.; Zhang, K.; Ye, Y.; Dai, L. J. N. A mixed-dimensional light-emitting diode based on a p-MoS 2 nanosheet and an n-CdSe nanowire. *Nanoscale* **2017**, *9* (46), 18175−18179.
(23) Zhao, B.; Wang, F.; Chen, H.; Zheng, L.; Su, L.; Zhao, D.; Fang, X. J. An ultrahigh responsivity (9.7 mA W− 1) self-powered solar-blind photodetector based on individual ZnO−Ga2O3 heterostructures. *Adv. Funct. Mater.* **2017**, *27* (17), 1700264.
(24) Higashiwaki, M.; Konishi, K.; Sasaki, K.; Goto, K.; Nomura, K.; Thieu, Q. T.; Togashi, R.; Murakami, H.; Kumagai, Y.; Monemar, B. J. A. P. L. Temperature-dependent capacitance−voltage and current−voltage characteristics of Pt/Ga2O3 (001) Schottky barrier diodes fabricated on n−−Ga2O3 drift layers grown by halide vapor phase epitaxy. *Appl. Phys. Lett.* **2016**, *108* (13), 133503.
(25) Villora, E. G.; Yamaga, M.; Inoue, T.; Yabasi, S.; Masui, Y.; Sugawara, T.; Fukuda, T. Optical spectroscopy study on β-Ga2O3. *Japanese journal of applied physics* **2002**, *41* (6A), L622.
(26) Guo, D.; Wu, Z.; Zhang, L.; Yang, T.; Hu, Q.; Lei, M.; Li, P.; Li, L.; Tang, W. J. A. P. L. Abnormal bipolar resistive switching behavior in a Pt/GaO1. 3/Pt structure. *Appl. Phys. Lett.* **2015**, *107* (3), 032104.
(27) Kumar, S.; Dhara, S.; Agarwal, R.; Singh, R. J. J. Study of photoconduction properties of CVD grown β-Ga2O3 nanowires. *J. Alloys Compd.* **2016**, *683*, 143−148.
(28) Tak, B. R.; Gupta, V.; Kapoor, A. K.; Chu, Y.-H.; Singh, R. J. A. Wearable gallium oxide solar-blind photodetectors on muscovite mica having ultrahigh photoresponsivity and detectivity with added high-temperature functionalities. *Applied Electronic Materials* **2019**, *1* (11), 2463−2470.
(29) Yang, G.; Jang, S.; Ren, F.; Pearton, S. J.; Kim, J. J. A. a. m. interfaces, Influence of high-energy proton irradiation on β-Ga2O3 nanobelt field-effect transistors. *ACS applied materials interfaces* **2017**, *9* (46), 40471−40476.
(30) Razeghi, M.; Park, J.-H.; McClintock, R.; Pavlidis, D.; Teherani, F. H.; Rogers, D. J.; Magill, B. A.; Khodaparast, G. A.; Xu, Y.; Wu, J. J. A review of the growth, doping, and applications of Beta-Ga2O3 thin films. *Oxide-Based Materials Devices IX* **2018**, *10533*, 21−44.
(31) Zhuo, R.; Wu, D.; Wang, Y.; Wu, E.; Jia, C.; Shi, Z.; Xu, T.; Tian, Y.; Li, X. A self-powered solar-blind photodetector based on a MoS 2/β-Ga 2 O 3 heterojunction. *Journal of Materials Chemistry C* **2018**, *6* (41), 10982−10986.
(32) Huan, Y.-W.; Xu, K.; Liu, W.-J.; Zhang, H.; Golosov, D. A.; Xia, C.-T.; Yu, H.-Y.; Wu, X.-H.; Sun, Q.-Q.; Ding, S.-J. J. Investigation of Band Alignment for Hybrid 2D-MoS 2/3D-β-Ga 2 O 3 Heterojunctions with Nitridation. *Nanoscale Res. Lett.* **2019**, *14* (1), 1−8.
(33) Kranert, C.; Sturm, C.; Schmidt-Grund, R.; Grundmann, M. J. Raman tensor elements of β-Ga2O3. *Sci. Rep.* **2016**, *6* (1), 1−9.
(34) Kumar, S.; Singh, R. Nanofunctional gallium oxide (Ga2O3) nanowires/nanostructures and their applications in nanodevices. *physica status solidi − Rapid Research Letters* **2013**, *7* (10), 781−792.
(35) Li, H.; Wu, J.; Yin, Z.; Zhang, H. J. Preparation and applications of mechanically exfoliated single-layer and multilayer MoS2 and WSe2 nanosheets. *Accounts of chemical research* **2014**, *47* (4), 1067−1075.
(36) Ebel, M. F.; Ebel, H. J. About the charging effect in X-ray photoelectron spectrometry. *J. Electron Spectrosc. Relat. Phenom.* **1974**, *3* (3), 169−180.
(37) Kim, I. S.; Sangwan, V. K.; Jariwala, D.; Wood, J. D.; Park, S.; Chen, K.-S.; Shi, F.; Ruiz-Zepeda, F.; Ponce, A.; Jose-Yacaman, M. J. A. n.; et al. Influence of stoichiometry on the optical and electrical properties of chemical vapor deposition derived MoS2. *ACS Nano* **2014**, *8* (10), 10551−10558.
(38) Mukherjee, S.; Maiti, R.; Midya, A.; Das, S.; Ray, S. K. J. A. P. Tunable direct bandgap optical transitions in MoS2 nanocrystals for photonic devices. *Acs Photonics* **2015**, *2* (6), 760−768.

(39) Tak, B.; Dewan, S.; Goyal, A.; Pathak, R.; Gupta, V.; Kapoor, A.; Nagarajan, S.; Singh, R. J. A. S. S. Point defects induced work function modulation of β-Ga2O3. *Appl. Surf. Sci.* **2019**, *465*, 973−978.
(40) Henck, H.; Aziza, Z. B.; Zill, O.; Pierucci, D.; Naylor, C. H.; Silly, M. G.; Gogneau, N.; Oehler, F.; Collin, S.; Brault, J. J. P. R. B.; et al. Interface dipole and band bending in the hybrid p− n heterojunction Mo S 2/GaN (0001). *Phys. Rev. B* **2017**, *96* (11), 115312.
(41) Kümmell, T.; Hutten, U.; Heyer, F.; Derr, K.; Neubieser, R.-M.; Quitsch, W.; Bacher, G. J. P. R. B. Carrier transfer across a 2D-3D semiconductor heterointerface: The role of momentum mismatch. *Phys. Rev. B* **2017**, *95* (8), 081304.
(42) Si, C.; Lin, Z.; Zhou, J.; Sun, Z. J. D. M. Controllable Schottky barrier in GaSe/graphene heterostructure: the role of interface dipole. *2D Materials* **2017**, *4* (1), 015027.
(43) Zdanowicz, E.; Herman, A. P.; Opołczyńska, K.; Gorantla, S.; Olszewski, W.; Serafińczuk, J.; Hommel, D.; Kudrawiec, R. Toward h-BN/GaN Schottky Diodes: Spectroscopic Study on the Electronic Phenomena at the Interface. *ACS Appl. Mater. Interfaces* **2022**, *14* (4), 6131−6137.
(44) Mohamed, M.; Irmscher, K.; Janowitz, C.; Galazka, Z.; Manzke, R.; Fornari, R. J. A. P. L. Schottky barrier height of Au on the transparent semiconducting oxide β-Ga2O3. *Appl. Phys. Lett.* **2012**, *101* (13), 132106.
(45) Kraut, E.; Grant, R.; Waldrop, J.; Kowalczyk, S. J. P. R. L. Precise determination of the valence-band edge in x-ray photo-emission spectra: application to measurement of semiconductor interface potentials. *Phys. Rev. Lett.* **1980**, *44* (24), 1620.
(46) Hinuma, Y.; Pizzi, G.; Kumagai, Y.; Oba, F.; Tanaka, I. J. C. M. S. Band structure diagram paths based on crystallography. *Comput. Mater. Sci.* **2017**, *128*, 140−184.
(47) Mishra, M.; Gundimeda, A.; Garg, T.; Dash, A.; Das, S.; Gupta, G. J. A. S. S. ZnO/GaN heterojunction based self-powered photodetectors: influence of interfacial states on UV sensing. *Appl. Surf. Sci.* **2019**, *478*, 1081−1089.
(48) Kung, S.-C.; van der Veer, W. E.; Yang, F.; Donavan, K. C.; Penner, R. M. J. N. l. 20 μs photocurrent response from lithographically patterned nanocrystalline cadmium selenide nano-wires. *Nano Lett.* **2010**, *10* (4), 1481−1485.
(49) Sharma, M.; Singh, A.; Aggarwal, P.; Singh, R. J. A. o. Large-Area Transfer of 2D TMDCs Assisted by a Water-Soluble Layer for Potential Device Applications. *ACS omega* **2022**, *7* (14), 11731−11741.
(50) Cui, S.; Mei, Z.; Zhang, Y.; Liang, H.; Du, X. J. A. O. M. Room-Temperature Fabricated Amorphous Ga2O3 High-Response-Speed Solar-Blind Photodetector on Rigid and Flexible Substrates. *Advanced Optical Materials* **2017**, *5* (19), 1700454.
(51) Lee, Y.; Park, S.; Kim, H.; Han, G. H.; Lee, Y. H.; Kim, J. Characterization of the structural defects in CVD-grown monolayered MoS2 using near-field photoluminescence imaging. *Nanoscale* **2015**, *7* (28), 11909−11914.
(52) Qi, J.; Lan, Y.-W.; Stieg, A. Z.; Chen, J.-H.; Zhong, Y.-L.; Li, L.-J.; Chen, C.-D.; Zhang, Y.; Wang, K. L. J. N. c. Piezoelectric effect in chemical vapour deposition-grown atomic-monolayer triangular molybdenum disulfide piezotronics. *Nat. Commun.* **2015**, *6* (1), 1−8.
(53) Garg, M.; Naik, T. R.; Pathak, C.; Nagarajan, S.; Rao, V. R.; Singh, R. J. A. P. L. Significant improvement in the electrical characteristics of Schottky barrier diodes on molecularly modified Gallium Nitride surfaces. *Appl. Phys. Lett.* **2018**, *112* (16), 163502.
(54) Yang, L.; Cui, X.; Zhang, J.; Wang, K.; Shen, M.; Zeng, S.; Dayeh, S. A.; Feng, L.; Xiang, B. J. S. r. Lattice strain effects on the optical properties of MoS2 nanosheets. *Sci. Rep.* **2014**, *4* (1), 1−7.
(55) Zhang, K.; Peng, M.; Wu, W.; Guo, J.; Gao, G.; Liu, Y.; Kou, J.; Wen, R.; Lei, Y.; Yu, A. J. M. H.; et al. A flexible p-CuO/n-MoS 2 heterojunction photodetector with enhanced photoresponse by the piezo-phototronic effect. *Materials Horizons* **2017**, *4* (2), 274−280.
(56) Li, J.; Wang, Z.; Wen, Y.; Chu, J.; Yin, L.; Cheng, R.; Lei, L.; He, P.; Jiang, C.; Feng, L. J. A. F. M. High-performance near-infrared photodetector based on ultrathin Bi2O2Se nanosheets. *Adv. Funct. Mater.* **2018**, *28* (10), 1706437.
(57) Liu, J.; Wang, H.; Li, X.; Chen, H.; Zhang, Z.; Pan, W.; Luo, G.; Yuan, C.; Ren, Y.; Lei, W. J. J. o. A. Compounds, High performance visible photodetectors based on thin two-dimensional Bi2Te3 nanoplates. *J. Alloys Compd.* **2019**, *798*, 656−664.
(58) Singh, A.; Sharma, M.; Singh, R. J. C. G. Design, NaCl-Assisted CVD Growth of Large-Area High-Quality Trilayer MoS2 and the Role of the Concentration Boundary Layer. *Crystal Growth Design* **2021**, *21* (9), 4940−4946.
(59) Tak, B. R.; Gupta, V.; Kapoor, A. K.; Chu, Y.-H.; Singh, R. J. A. A. E. M. Wearable gallium oxide solar-blind photodetectors on muscovite mica having ultrahigh photoresponsivity and detectivity with added high-temperature functionalities. *ACS Applied Electronic Materials* **2019**, *1* (11), 2463−2470.
(60) Sharma, M.; Aggarwal, P.; Singh, A.; Kaushik, S.; Singh, R. Flexible, Transparent, and Broadband Trilayer Photodetectors Based on MoS2/WS2 Nanostructures. *ACS Applied Nano Materials* **2022**, *5* (9), 13637−13648.
(61) Blöchl, P. E.; Jepsen, O.; Andersen, O. K. J. P. R. B. Improved tetrahedron method for Brillouin-zone integrations. *Phys. Rev. B* **1994**, *49* (23), 16223.
(62) Botana, A. S.; Norman, M. R. J. P. R. M. Electronic structure and magnetism of transition metal dihalides: bulk to monolayer. *Physical Review Materials* **2019**, *3* (4), 044001.
(63) Sham, L. J.; Kohn, W. J. P. R. One-particle properties of an inhomogeneous interacting electron gas. *Phys. Rev.* **1966**, *145* (2), 561.
(64) Tao, J.; Perdew, J. P.; Tang, H.; Shahi, C. Origin of the size-dependence of the equilibrium van der Waals binding between nanostructures. *J. Chem. Phys.* **2018**, *148* (7), 074110.
(65) Heyd, J.; Scuseria, G. E.; Ernzerhof, M. Hybrid functionals based on a screened Coulomb potential. *J. Chem. Phys.* **2003**, *118* (18), 8207−8215.
(66) Tkatchenko, A.; Scheffler, M. J. P. r. l. Accurate molecular van der Waals interactions from ground-state electron density and free-atom reference data. *Physical review letters* **2009**, *102* (7), 073005.